Polarized imaging of visible synchrotron emission from runaway electron plateaus in DIII-D

Ž. Popović[1,a)], E.M. Hollmann[1], D. Del-Castillo-Negrete[2], I. Bykov[3], R.A. Moyer[1], J.L. Herfindal[2], D. Shiraki[2], N.W. Eidietis[3], C. Paz-Soldan[4], A. Lvovskiy[3]

[1] University of California – San Diego, 9500 Gilman Drive, La Jolla, CA 92093-0417, USA
[2] Oak Ridge National Laboratory, PO Box 2008, Oak Ridge, TN 37831, USA
[3] General Atomics, PO Box 85608, San Diego, CA 92186-5608, USA
[4] Department of Applied Physics and Applied Mathematics, Columbia University, New York, NY 10024, USA

a) Corresponding author, zpopovic@ucsd.edu

Abstract

A new approach to estimate the pitch angle of highly energetic post-disruption runaway electrons is presented by imaging the polarized runaway electron synchrotron emission. The vertical to horizontal polarization ratio is found to range between 3 and 14 in image-average studies looking at repeated shots as well as the polarization in a single discharge. Numerical studies with guiding center and full orbit simulations performed with the SOFT and KORC codes are given and compared to experiment. The pitch angle evolution analyzed using a 1D impurity diffusion model in combination with kinetic simulations is also presented. These studies find agreement in the magnitude of the pitch angle, but not in the temporal rate of change of pitch angle. The measured pitch angle evolution timescale of order 50 ms falls between a modeled timescale of 20 ms in an equilibrium model and >>100 ms in a non-equilibrium model.

I. Introduction

Loss of confinement of relativistic (~ 10-100 MeV) runaway electrons (REs) and deposition of their energy onto the first wall structures following disruptions could become detrimental to the safe operation of future tokamak-based fusion devices[1]. Understanding the formation, amplification, and loss of REs in tokamaks

is therefore an active area of research[2]. In tokamak experiments, REs are diagnosed with a variety of passive radiation diagnostics (soft X-ray emission, hard X-ray emission, and electron cyclotron emission)[3]; relative to these measurements, visible synchrotron emission (SE) gives excellent information of spatial structure (~ 1 cm) with still very good time resolution (> 10 kHz)[4]. Additionally, due to the strong forward-beaming of SE from REs, the measurement is relatively localized to the tangency plane, not line-integrated through the whole plasma volume like other passive radiation diagnostics[5].

A disadvantage of SE as a RE diagnostic is that it measures only a fairly small region of phase space, i.e. REs with fairly high energy and pitch angle[6]. Additionally, quantitative interpretation of SE is challenging because the SE brightness depends on both runaway number density (n_{RE}) and pitch angle (θ), so an independent measure or simulation of pitch angle is required to interpret data[7]. SE has been interpreted by assuming a single pitch angle at each energy, i.e. by reducing the actual 2D phase space of electron momentum and pitch angle into a 1D phase space[8].

A promising approach to isolate pitch angle of REs and thus decrease uncertainty when analyzing SE is to look at the linear polarization of the SE[9]. The polarization map of a sample RE SE image with spatially homogenous mono-energetic RE distribution and a fixed pitch angle in a circular cross section tokamak was first calculated in Ref. [10]. It was shown that the degree of linear polarization is determined by the RE pitch angle and energy and, for parameters of mid-sized tokamaks, it ranges from 0 - 80%. Additionally, the linear polarization direction across the plasma cross section could vary from vertical to horizontal (with unpolarized regions between) depending on the pitch angle values. The first experimental measurement of the SE polarization from REs in a tokamak was done during a low-density non-disruptive plasma current flattop in Alcator C-Mod[9]. The Motional Stark Effect (MSE) diagnostic was used to measure the SE polarization over a narrow view covering different radial positions across the radial midplane to confirm that the SE was strongly polarized, and a sudden spatial change in polarization between horizontal and vertical directions was observed moving outward along the radial direction.

In the study presented here, polarized full cross-section images of visible (790 nm) SE are recorded during RE plateaus (i.e., post-disruption RE beams) in DIII-D discharges. This differs from previous work in that entire 2D images are measured (as opposed to 1D radial arrays). It is found that throughout the cross-section the RE SE tends to be more vertically polarized, and that the (vertical vs. horizontal) polarization imbalance increases with pitch angle, thus suggesting a possible method to measure RE pitch angle and its spatial dependence (at least at the very high energies responsible for visible SE). The images are compared with synthetic images obtained in simulations with the Synchrotron-detecting Orbit Following Toolkit

(SOFT[11]) and a new version of the Kinetic Orbit Runaway electron Code (KORC[12]) synchrotron emission diagnostic that includes analysis of synchrotron polarization. Also, for toroidally symmetric systems (like the ones of interest here) the new version of KORC uses a faster and more accurate numerical method that conserves exactly the angular momentum and uses the symmetry to increase the efficiency of the Monte-Carlo sampling. Furthermore, the evolution of SE following D_2 massive gas injection (MGI) into a typical DIII-D RE plateau is studied. D_2 MGI is thought to rapidly change the RE pitch angle scattering and thus provides an excellent test bed for the study of RE pitch angle response to changes in pitch angle scattering rate. The recovered pitch angle time evolution is compared with simulations based on a kinetic test particle model combined with a 1-D impurity radial diffusion. The approximate values of the measured pitch angle are found to be in reasonable agreement with the simulations; however, the observed rate of change of pitch angle is presently poorly predicted by the simulations.

The paper is organized as follows: Section II gives a brief background on SE as well as an experimental overview, Section III presents data on polarized SE imaging, Section IV presents simulations of polarized SE imaging, Section V presents attempts to estimate the RE pitch angle time evolution using SE polarization and comparisons to kinetic modeling, and, finally, Section VI contains a brief discussion.

II. Experimental background

a. Conceptual picture

The polarization of SE is determined by the trajectory of a relativistic RE, where the dominant electric field component lies parallel to the electron acceleration, seen in the local coordinate system, Fig. 1(a)[13]. The measured SE radiation spot is an image formed by an average over many REs and their gyro-orbits. Figure 1(b) gives a schematic representation of the typical crescent-shaped synchrotron spot observed for a RE beam in the poloidal plane of a tokamak, where P_Z and P_X denote the vertically and horizontally polarized components of SE brightness, respectively. For deeper understanding, two limiting cases can be considered. First, if the runaway electron is just gyro-orbiting around a point and its SE is observed down the axis of electron rotation, the polarization would be radially inward toward the point (with equal spatially averaged polarizations $\langle P_X \rangle$ and $\langle P_Z \rangle$). In the other limit, where the RE is just going around toroidally (no gyromotion), the polarization would be in the plane of the orbit (P_X). In the complicated case where the REs have spiral orbits with

larger pitch angle on the inboard side, a complex (P_X, P_Z) structure is formed which needs to be resolved by simulations.

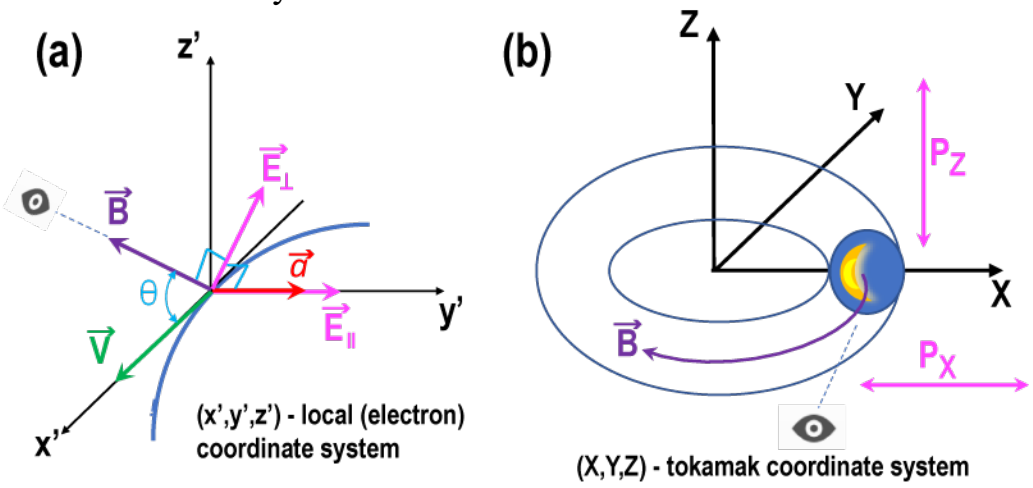

Figure 1. (a) Schematic frame of reference showing the electric field components of the synchrotron emission for an electron along its trajectory, and (b) vertically (P_Z) and horizontally (P_X) polarized brightness observed for an ensemble of REs (a RE beam) in a tokamak.

b. Description of experiment

These experiments were conducted on the DIII-D tokamak[14]. Figure 2(a) shows the placement and viewing direction of the main diagnostics used in the experiments. The primary diagnostics are tangentially viewing fast-framing visible cameras at 90º and 225º. Figure 2(b) shows time traces of the typical plasma parameters for three post-disruption RE plateau discharges of interest. In these experiments, a steady state RE plateau was created by injection of an Ar pellet at time t = 1200 ms, leading to a rapid shutdown and formation of a RE current plateau, which is then current stabilized at $I_P \approx 275$ kA and position stabilized to avoid vertical drift of the RE current channel. In these "standard" RE plateaus, the dominant impurity is Ar and visible line emission is dominated by Ar-I and Ar-II lines. D_2 MGI is employed later in the plateau (at t = 1500 ms) in two of the shots shown here (#175768 and #175775) for the purpose of net expulsion of Ar impurities[15]. This Ar purge should lead to a sudden decrease in RE pitch angle scattering, so it is expected that there would be a decrease in pitch angle values, which would be accompanied by a decrease in synchrotron emission.

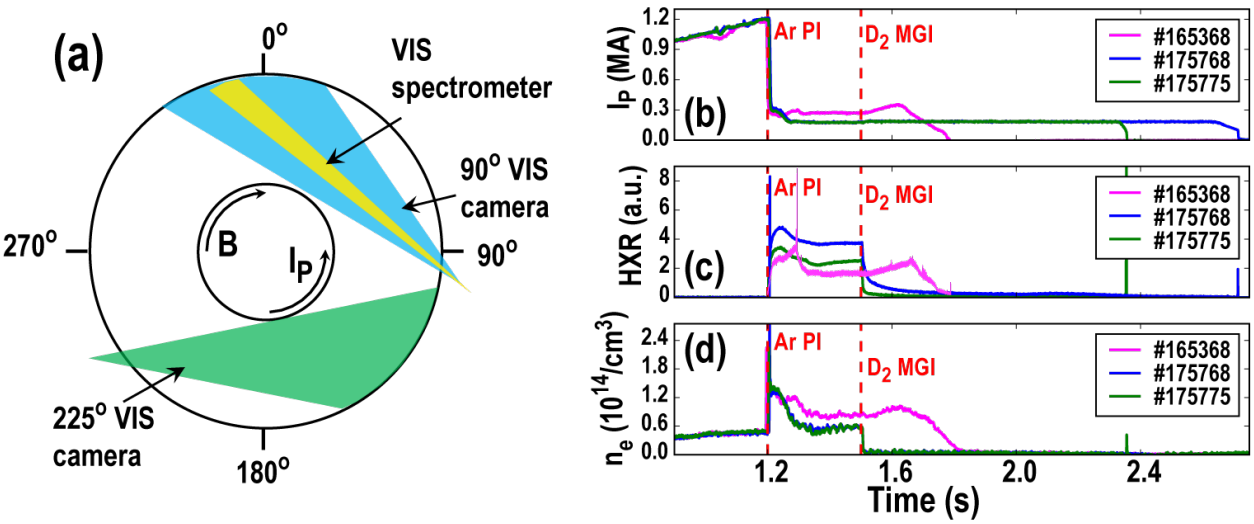

Figure 2. (a) Top view schematic of DIII-D tokamak with fields of view of visible camera and visible spectrometer diagnostics, and time traces showing (b) plasma current (I_p), (c) hard X-ray (HXR) scintillator signal, and (d) electron density (n_e) for the three discharges. The red dashed lines indicate the times of Ar and D_2 (shots #175768 and #175775 only) injections.

In DIII-D, RE synchrotron emission is expected to peak in the mid-infrared wavelength (~5 μm) region but significant SE brightness is typically still observed in the visible light region[16]. For either visible camera, SE is isolated spectrally by using a 790 nm bandpass filter with 10 nm bandpass. This spectral bandpass is chosen to maximize SE (which rises strongly with increasing wavelength in the visible region) within the spectral sensitivity of the camera, while also avoiding strong Ar or D emission lines. Sample visible spectra from a tangentially-viewing (with roughly centered view and 10 cm spot size on the middle of the plasma) visible spectrometer are shown in Fig. 3. These spectra were taken with a polarizer mounted in front of the spectrometer collimator, showing stronger vertical polarization (about 6.5×), but no clear difference in spectral shape between different polarizations. The data was taken after D_2 MGI, so D-I lines are dominant. Similar SE spectra have been taken for normal (pre- D_2 MGI) RE plateaus, showing that the 790 nm region is also free of strong Ar-I and Ar-II lines[4].

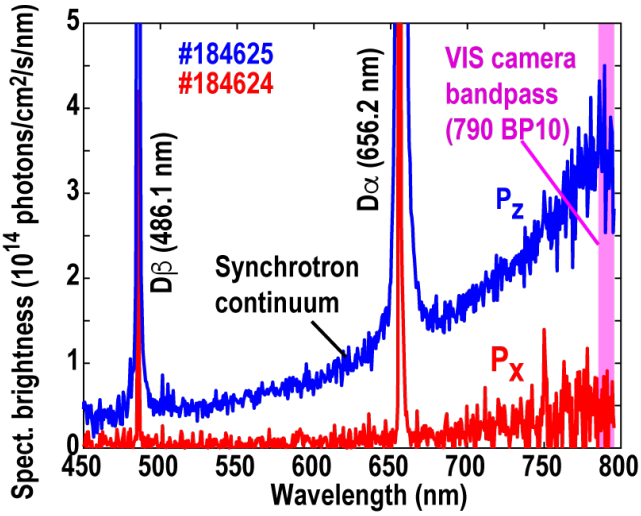

Figure 3. Survey spectrometer spectra for vertical (P_Z) and horizontal polarization (P_X) collected using a collimated view at the 90º port. Fast camera imaging wavelength range is indicated by pink vertical band.

Ideally, vertically polarized, horizontally polarized, and unpolarized SE images could be obtained on the same plasma shot for detailed comparison with simulations. Due to the limitation of having only two tangential visible cameras, however, this is not presently possible. Two different analysis approaches are used for studying SE here: (i) nominally repeat shots are taken and the linear polarizer in front of one of the cameras is rotated shot-to-shot, or (ii) one camera is left vertically polarized while the other unpolarized and the (not measured) horizontal polarized image is then estimated for the same shot by subtracting the vertical polarized image from the unpolarized image. Both analysis methods have disadvantages. Method (i) has the disadvantage that shot-to-shot repeatability of RE plateaus is not perfect. This can be seen in Fig. 2, where the shots are, prior to t = 1.5 s, nominal repeat shots with similar Ar pellet size, same pre-fill density, etc. However, it can be seen that there are still significant shot-to-shot variations in parameters such as (b) plasma current, (c) hard X-ray emission, and (d) free electron density. Both methods also require good image spatial and brightness calibrations. Brightness calibration, especially, is challenging in these experiments due to HXR degradation of the camera fiber bundles. On average, the HXRs cause a fiber bundle transmission degradation of approximately 2× during the course of each RE plateau discharge. For the analysis presented in this work, a fiber bundle degradation factor which corrects for the loss of transmission during each shot was calculated for each image by using the HXR scintillator signal levels as a proxy for HXRs causing the bundle darkening. Other corrections are applied together with the bundle darkening factor, such as window transmission and dark field background calibration, while background emission is assumed to be negligible in the SE bandpass region[4] relative

to the absolute error of the chosen method. For method (ii), spatial calibration is especially challenging, since two different cameras are used and the images are subtracted from each other. Spatial calibration is less crucial for method (i), where a single camera can be used and can be held fixed while the linear polarizer is rotated.

III. Fast camera imaging of polarized RE synchrotron emission spot in DIII-D

As mentioned in the previous section, unpolarized, horizontally polarized, and vertically polarized SE images are desired under the same conditions for comparisons with simulations. With the two cameras available here, these could be obtained either by (i) using repeat shots or (ii) by subtracting a polarized image from an unpolarized image. Figure 4 shows an example of images obtained using method (i) using the 90º camera and rotating the linear polarizer shot-to-shot. Figure 4(a) shows the distinctive crescent shape of an unpolarized SE spot, while Figs. 4(b,c) correspond to the horizontally (P_X) and vertically (P_Z) polarized cases, respectively. Strong differences in the SE spot shape and brightness level are observed between the two polarized images.

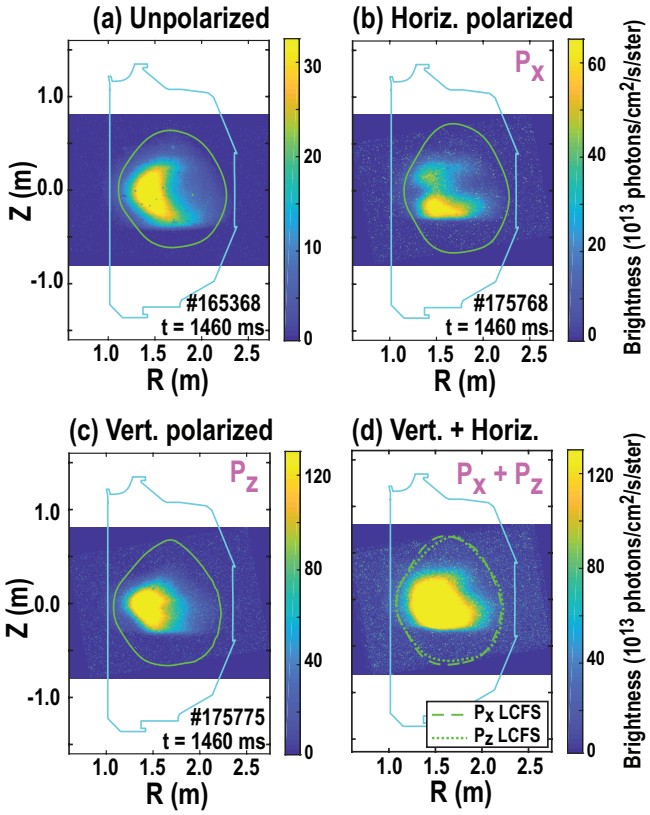

Figure 4. Fast camera images of the RE SE spot in three typical DIII-D RE plateau discharges showing (a) unpolarized, (b) horizontally linearly polarized (P_X), and (c) vertically linearly polarized (P_Z) brightness. Image (d) shows a sum brightness of the two polarized images. Green solid (dashed in (d)) curves in each image indicate the last closed flux surface from JFIT current filament reconstructions, relative to the vacuum vessel outline (shown in cyan).

As discussed above, shot-to-shot reproducibility is not perfect in RE plateau shots so the method of rotating a polarizer between shots on a single camera is imperfect. As a clear demonstration of this, summing the two polarized images, Fig. 4(b) and Fig. 4(c) does not accurately recover the unpolarized image Fig. 4(a), yet rather results in a distorted circular SE spot, Fig. 4(d). Using two cameras on the same shot removes this issue of shot-to-shot repeatability. Figure 5 shows (a) an unpolarized image (taken with 225º camera), (c) a vertically polarized image (taken with 90º camera) on the same shot, and (b) a horizontally polarized image constructed by subtracting image (c) from image (a). Because of the uncertainties in absolute calibration, the vertically polarized image is scaled so that the resulting subtracted image has a minimum value of zero (this is based on the expectation that some parts of the image will be fully vertically polarized).

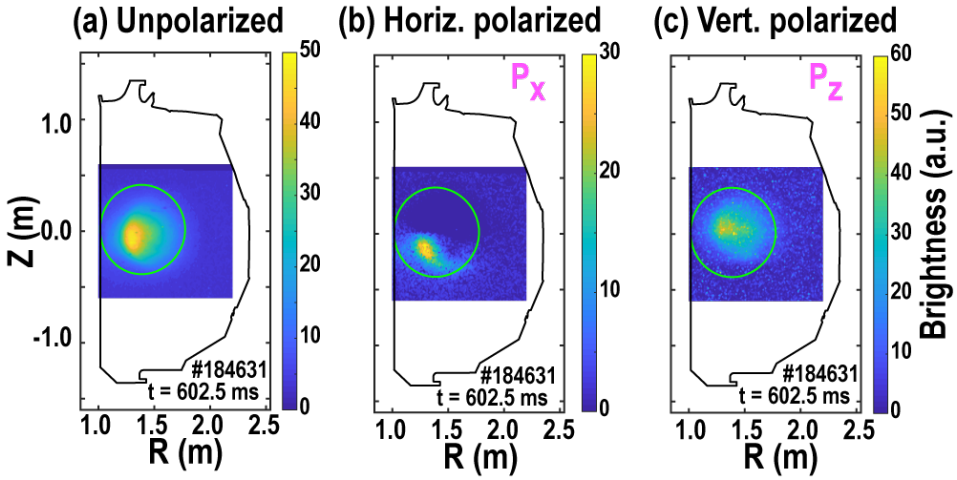

Figure 5. Synchrotron emission from a RE beam imaged at two toroidal locations (a) without and (c) with a polarizer (P_Z) during a single discharge; (b) Complementary polarization (P_X) reconstructed from experimental images. The green curve is the last closed flux surface estimated from EFIT.

IV. Synthetic images generated using SOFT and KORC

The Synchrotron-detecting Orbit Following Toolkit (SOFT[11]) and a new optimized version of the Kinetic Orbit Runaway electron Code (KORC[12]) synchrotron diagnostic including polarization (details of which will be presented in a forthcoming publication) are the two principal codes with the capability to model tokamak SE images. Both codes were used here, incorporating the experimental magnetic geometry information from JFIT, and while SOFT uses a guiding-center (GC) hollow cone approximation described more in-depth below, KORC uses the full orbit dynamics and the full geometric angular dependence of the synchrotron emission.

SOFT is a synthetic diagnostic toolkit used for modeling of the synchrotron radiation spot for a given device geometry and detector placement. It solves the guiding-center equations of motion for a given electron distribution function, while assuming a cone model of synchrotron radiation in this case as a means to optimize computation, which can be interpreted as though the GC emits synchrotron radiation in a hollow cone of opening angle θ around its direction of motion[11]. Figure 6 shows SOFT images obtained for a mono-energetic ($E = 20$ MeV) and mono-pitch ($\theta = 0.2$ rad) RE beam, where a quadratic safety factor q profile ($q(0) = 5$, $q(1) = 20$, estimated from EFIT reconstruction) has been assumed. Given the above approximations, the modeled polarized and unpolarized SE spots resemble the experimental images of Figs. 4, 5 reasonably well, capturing the asymmetry in the horizontally polarized case as well as returning the polarization ratio (Sec. V) in the same order of magnitude, $\langle P_Z \rangle / \langle P_X \rangle \approx 7$.

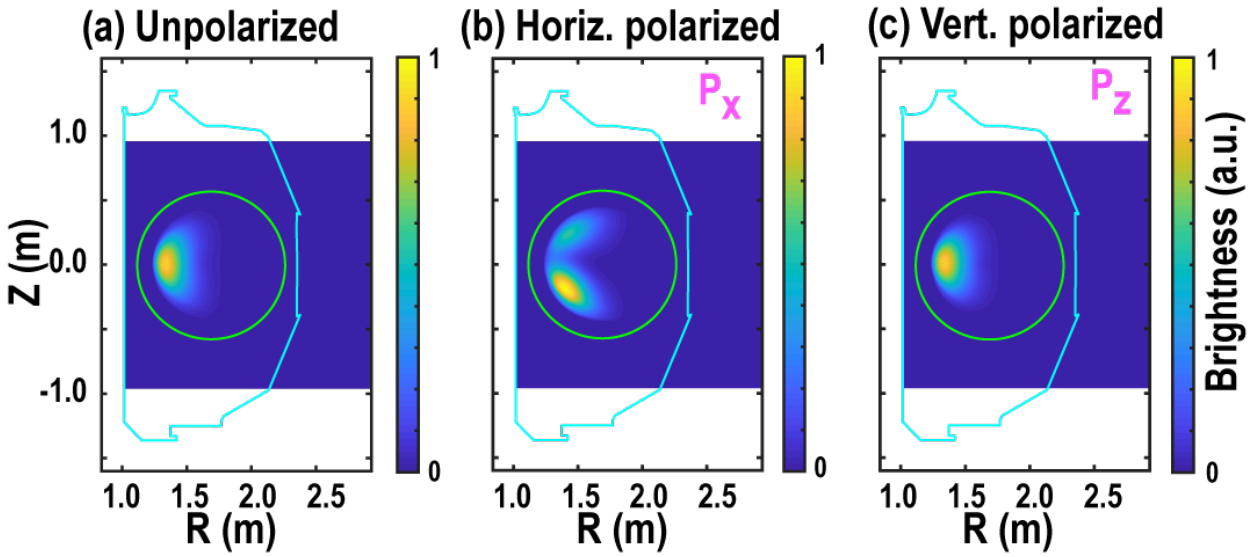

Figure 6. Synthetic images from SOFT for a mono-energetic and mono-pitch RE population: (a) unpolarized image, (b) horizontally polarized image, and (c) vertically polarized image. Note: the images were generated assuming a 0-order Bessel function of the first kind for radial density profile in SOFT.

KORC incorporates full orbit effects and computes the individual electron contributions to the SE and its polarization, taking into account the spectral and full angular distributions, as well as optical and geometric properties of the camera. For a given electron distribution function initial condition, KORC simulations start by running the orbits of a large ensemble of electrons. This eliminates fast transient effects, including prompt losses and collisionless pitch angle dispersion[17], and provides a kinematically consistent (in the collisionless timescale) electron distribution that is used for the computation of the synchrotron radiation polarization. As in SOFT, in these simulations KORC used a mono-energetic (E = 20 MeV) and mono-pitch (θ = 0.2 rad) RE beam as initial condition, and the same magnetic configuration as deduced from experiment ($q(0)$ = 5, $q(1)$ = 20). In principle, there can be a difference between the initial and the post-transient distributions reflected in the beam position and/or the spread of the pitch angle. However, for the energies considered in the KORC calculations presented in this paper the difference is not significant for the comparisons to the experimental images. However, as discussed in Sec.VI, this can be of relevance in a quantitative detailed comparison between KORC and SOFT, which is outside the scope of the present paper.

The resulting images for the three cases are shown in Figure 7, also displaying similarities with the main structural features observed in the experiment. The polarization ratio $\langle P_Z \rangle / \langle P_X \rangle$ in this case is found to be ≈ 5.8. In both KORC and SOFT simulations, the image structure and brightness of polarized and unpolarized SE images is found to be highly sensitive to pitch angle, with lower sensitivity to RE energy and observed wavelength range.

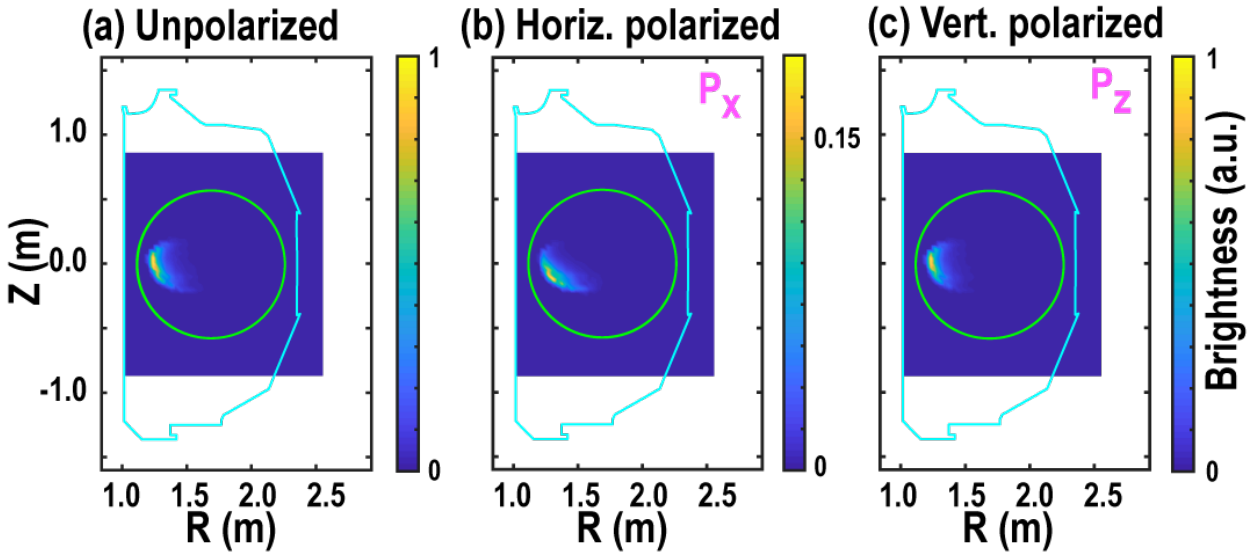

Figure 7. KORC generated camera images using a mono-energetic and mono-pitch RE distribution and full orbit calculation: (a) unpolarized, (b) horizontally and (c) vertically polarized RE SE brightness. The brightness scale has been normalized to the magnitude of the brightness of the unpolarized image.

V. RE pitch angle from polarized synchrotron brightness

In this section, global trends of P_Z and P_X as a function of time and the potential use of their ratio to estimate of RE pitch angle is investigated. For these purposes, image structure is neglected, and spatial averages over the entire image are used when discussing polarized brightness, i.e. $< P_Z > = \frac{1}{S}\int P_Z \, dx \, dz$ and $< P_X > = \frac{1}{S}\int P_X \, dx \, dz$, where x and z are image coordinates and S is total image area.

Figure 8 shows a $<P_Z>/<P_X>$ scan in SOFT and KORC over typical pitch angle values for three wavelengths, illustrating the effect of full orbit calculation vs. GC approximation. The lower polarization ratios in KORC might be due to geometry and orbit effects not captured in SOFT simulations. Furthermore, the GC approximation falls short for very high energies when the electron Larmor radius reaches the order of magnitude of the lengths of magnetic field variations[18]. The figure also demonstrates that polarization trends are not strongly dependent on imaging wavelength, i.e., similar results are expected if imaging at 790 nm (as is done here) or at 600 nm. The wavelengths chosen for Fig. 8 (600, 790, and 2000 nm) correspond roughly to wavelengths used in previous studies of SE measurement in tokamaks (using MSE, visible cameras, or IR cameras). The RE beam radius in both SOFT and KORC for these runs is initiated at 0.7 times the minor radius a, with linear and uniform radial profiles. This is expected to be a reasonable guess for the RE beam radius, but is nevertheless a source of uncertainty in the simulations. For example, assuming a RE beam radius of 0.4 a would change the ratio $<P_Z>/<P_X>$ by up to 50% for a given RE pitch angle and energy set calculated in SOFT. Loss of confinement also plays an important role in KORC calculations. Specifically, as mentioned before, to use a kinematically consistent distribution for radiation computation, KORC first runs the orbits of the given initial condition to eliminate transients. During this process, loss of confinement can reduce the effective radius of the RE beam. In particular, for the relatively high values of the q profile parameters used in the simulations, at 30 MeV most of the REs in KORC are lost due to drifts towards the low-field side, which is why this case is not included in Fig. 8.

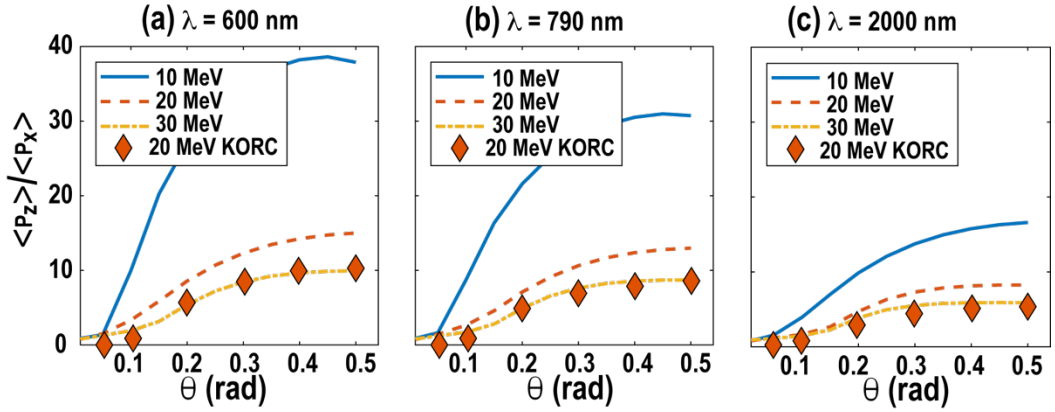

Figure 8. Comparison of the spatially averaged polarization ratio vs. pitch angle calculated using SOFT (lines) and KORC (symbols) for several mono-energetic distributions. Imaging wavelengths simulated are (a) 600 nm, (b) 790 nm, and (c) 2000 nm.

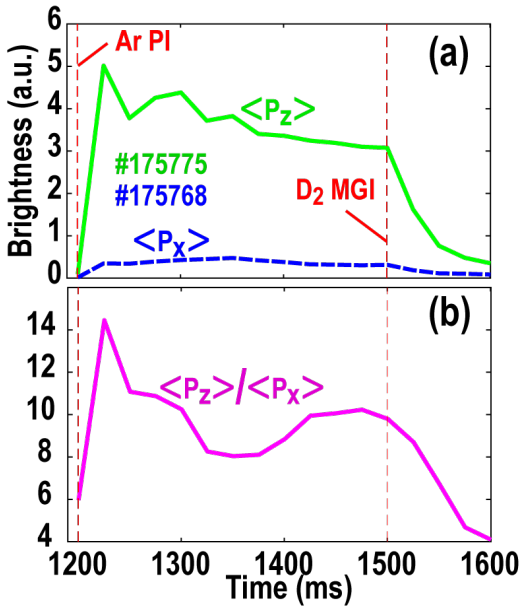

Figure 9. Time traces for two shots with D_2 MGI at t = 1.5 s cases showing (a) image-average polarized SE brightnesses $\langle P_Z \rangle$, and $\langle P_X \rangle$, as well as (b) the ratio $\langle P_Z \rangle / \langle P_X \rangle$. Red dashed lines mark the times of disruption-inducing Ar pellet injection and D_2 MGI.

Both the drop in total SE brightness $\langle P_X \rangle + \langle P_Z \rangle$ of Fig. 9(a), as well as the drop in the ratio $\langle P_Z \rangle / \langle P_X \rangle$ of Fig. 9(b) are believed to dominantly be the result of decreasing RE pitch angle θ. This is supported both by kinetic simulation of the RE pitch angle and distribution function, as well as by the SOFT modeling of $\langle P_Z \rangle / \langle P_X \rangle$. This is shown in Fig. 10, where time traces of (a) total SE brightness

$\langle P_X \rangle + \langle P_Z \rangle$ and (b) RE pitch angle θ are shown as a function of time following D_2 MGI. The "measured" pitch angle θ of Fig. 10(b) is the pitch angle inferred from the measured $\langle P_Z \rangle / \langle P_X \rangle$ and using the SOFT scaling of Fig. 8(b) for 20 MeV. From Fig. 8, the energy dependence in $\langle P_Z \rangle / \langle P_X \rangle$ is only strong at around 10 MeV but is not strong in the vicinity of 20 – 30 MeV. At the same time, the pitch angle dependence for 20 MeV is quite strong in the expected range of pitch angles $\theta \sim 0.1$ – 0.3 rad. Visible SE in DIII-D RE plateaus is thought to be dominated by ~ 20 – 30 MeV REs with very little contribution from the ~ 10 MeV population[8]. As a result, the assumption of constant 20 MeV is made for the purposes of interpreting $\langle P_Z \rangle / \langle P_X \rangle$. It can be seen in Fig. 10(b) that the inferred "measured" RE pitch angle does appear to drop from $\theta \sim 0.25$ to $\theta \sim 0.1$ in the 80 ms following D_2 MGI.

The "model" curves of Fig. 10 show image-average SE brightness and pitch angle estimated from kinetic simulations. First, a 1D impurity diffusion model is used to estimate the evolution of the impurity radial profile following D_2 MGI[15]. In this model, the D_2 deposition rate into the vacuum vessel from the low field side (somewhat above the midplane) is based on numerically validated analytical modeling of gas flow down a narrow guide tube into vacuum[19]. Then, a 2D (1D space and 1D energy, with a single pitch angle at each energy) kinetic test particle model incorporating the 1D estimated impurity profile is used to estimate the RE distribution function, pitch angle, and synchrotron emission brightness[20]. The experimentally measured loop voltage is used in the simulations. The pitch angle plotted in Fig. 10(b) is the SE-weighted pitch angle, i.e. the pitch angle of the REs dominating the SE emission. Two different approximations are used for the pitch angle in the kinetic simulations: the "equilibrium" simulations assume instantaneous equilibration between electric field force and pitch angle scattering on pitch angle; this results in very rapid (~ 20 ms) equilibration of the SE brightness. "Non-equilibrium" simulations still use a 1D phase space approximation (assuming a single pitch angle at each energy) but allow pitch angle to evolve in time according to the pitch angle scattering rate. The pitch angle scattering rate is very low at the high energies (15 MeV+) dominating SE, resulting in an extremely slow (> 100 ms) equilibration timescale for these simulations. As can be seen in Fig. 10(b), the modeled pitch angles are similar in magnitude to the "measured" ones, but the "measured" pitch angle evolution timescale of order 50 ms falls between the modeled timescales in the equilibrium model (~ 20 ms) and non-equilibrium model (> 100 ms).

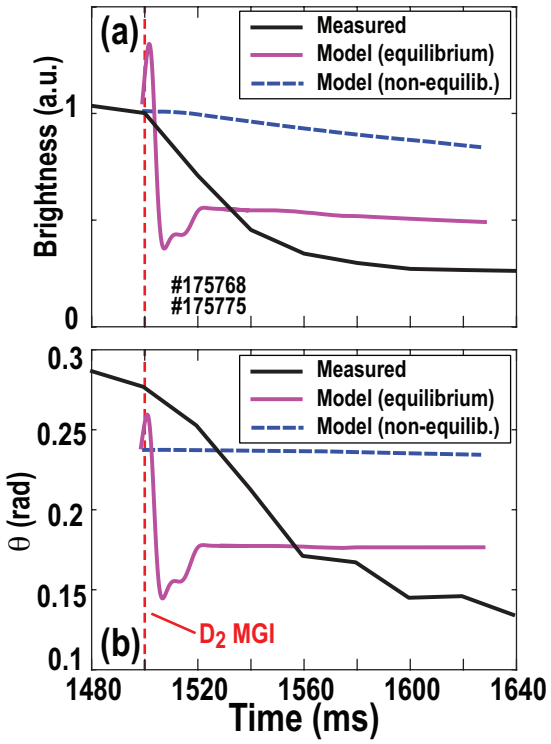

Figure 10. Experimentally measured/inferred and simulated: (a) SE brightness vs. time and (b) pitch angle vs. time. The 1-D impurity diffusion model does not recover the timescale observed in experiment after the D_2 MGI.

VI. Discussion and future work

Polarization of visible SE from REs was studied in post-disruption RE plateaus in DIII-D discharges with the goal of gaining information about RE pitch angle. Visible images from fast framing cameras with a linear polarizer were analyzed and showed that the RE plateau synchrotron emission is predominantly linearly polarized along the vertical direction. The image-average intensity ratio between vertical and horizontal SE brightness $\langle P_Z \rangle / \langle P_X \rangle$ was measured to be between 3 – 14. Two different approaches for comparing SE polarizations were presented: shot-to-shot repeats and single shot dual port imaging, both with advantages and disadvantages. The RE beam SE spot has been observed to take on the previously observed characteristic crescent shape, while the weaker polarization P_X formed a highly rotated and weakened crescent.

Leading synthetic SE image codes were used to generate simulated images for mono-energy and mono-pitch angle runaway distributions under a guiding-center assumption (SOFT) and using full orbit simulations (KORC). Although detailed

comparisons between measured and simulated images were not pursued here, future work will focus on more quantitative comparisons including, for example, spatial maps of the local polarization ratio P_Z/P_X.

SOFT and KORC were also used to parametrize the image-average polarization ratio $\langle P_Z \rangle / \langle P_X \rangle$ dependence on RE pitch angle. The SE polarization ratio was found to be a promising method for studying RE pitch angle evolution. For example, the drop in the $\langle P_Z \rangle / \langle P_X \rangle$ ratio during D_2 MGI was interpreted as a drop in the pitch angle θ, due to a pitch angle scattering decrease caused by a D_2 purge of argon from the plasma. This interpretation was qualitatively supported by kinetic simulations, with pitch angle values recovered from experiment and simulations agreeing within a factor of roughly 2, although the measured timescale of the pitch angle evolution was poorly reproduced by simulations. This disagreement in timescales suggests that some of the fundamental dynamics of the experiment are not being well-simulated. One obvious candidate is drift-orbit loss: this is included in a very crude way in the present model; however, the distribution function at high energies is expected to be strongly affected by drift orbit loss in these plasmas, so an accurate treatment of drift orbit loss may be required to accurately capture the time evolution of SE and its polarization. A different possibility may be that pitch angle scattering from wave-particle interactions could be causing this effect. Future simulations will attempt to better evaluate these different possibilities.

Although promising agreement between SOFT and KORC simulations was observed, further work is needed to understand the details of quantitative discrepancies. For example, the polarization ratios (Fig. 8) are systematically higher in SOFT than in KORC. What we know is that whereas KORC uses full orbit and full angle radiation dependences, SOFT uses the guiding center and, in this work, the radiation cone model approximations. There are also potential differences on the details regarding the implementation of the initial conditions, and the role of transients that can lead to the rapid loss of confinement and collisionless pitch angle dispersion. In particular, since the pitch angle is not a constant of motion and (depending on the energy) the beam might exhibit a fast outward shift (or be deconfined), in KORC the given mono-pitch mono-energy initial condition is first evolved in a very short (collisionless) timescale to eliminate fast transient effects. As discussed before, there might be a difference between the initial and the post transient distributions reflected in the beam position and/or the spread of the pitch angle (collisionless dispersion). What is not known yet is which one of the above mentioned differences between the two codes is the dominant factor. Addressing this question is outside the scope of the present paper and will be considered in a future publication.

Acknowledgements

The authors gratefully acknowledge assistance with SOFT from M. Hoppe and L. Stagner. This work was supported in part by the U.S. Department of Energy, Office of Science, Office of Fusion Energy Sciences, using the DIII-D National Fusion Facility, a DOE Office of Science user facility, under Awards DE-FG02-07ER54917, DE-FC02-04ER54698, DE-AC05-00OR22725, DE-AC52-07NA27344, DE-FG02-04ER54744, and DE-AC05-06OR23100. D. d.-C.-N. was sponsored by the U.S. Department of Energy, Office of Science, Office of Advanced Scientific Computing Research and Office of Fusion Energy Science, Scientific Discovery through Advanced Computing (SciDAC) program, at the Oak Ridge National Laboratory, which is operated by UT-Battelle, LLC, for the U.S. Department of Energy under Contract DE-AC05-00OR22725.

Data Availability

The data that supports the findings of this study are available from the corresponding author upon reasonable request. Additionally, DIII-D data shown in this paper can be obtained in digital format by following the links at Ref [21].

References

[1] M. Lehnen, K. Aleynikova, P.B. Aleynikov, D.J. Campbell, P. Drewelow, N.W. Eidietis, Yu. Gasparyan, R.S. Granetz, Y. Gribov, N. Hartmann, E.M. Hollmann, V.A. Izzo, S. Jachmich, S.H. Kim, M. Kocan, H.R. Koslowski, D. Kovalenko, U.

Kreuzi, A. Loarte, S. Maruyama, G.F. Matthews, P.B. Parks, G. Pautasso, R.A. Pitts, C. Reux, V. Riccardo, R. Roccella, J.A. Snipes, A.J. Thornton, P.C. de Vries, and EFDA JET contributors, J. Nucl. Mater. 463, 39 (2015).
[2] E.M. Hollmann, P.B. Aleynikov, T. Fülöp, D.A. Humphreys, V.A. Izzo, M. Lehnen, V.E. Lukash, G. Papp, G. Pautasso, F. Saint-Laurent, and J.A. Snipes, Phys. Plasmas 22, 021802 (2015).
[3] B.N. Breizman, P. Aleynikov, E.M. Hollmann, and M. Lehnen, Nucl. Fusion 59, 083001 (2019).
[4] J.H. Yu, E.M. Hollmann, N. Commaux, N.W. Eidietis, D.A. Humphreys, A.N. James, T.C. Jernigan, and R.A. Moyer, Phys. Plasmas 20, 042113 (2013).
[5] K.H. Finken, J.G. Watkins, D. Rusbuldt, W.J. Corbett, K.H. Dippel, D.M. Goebel, and R.A. Moyer, Nucl. Fusion 30, 859 (1990).
[6] M. Hoppe, L. Hesslow, O. Embreus, L. Unnerfelt, G. Papp, I. Pusztai, T. Fulop, O. Lexell, T. Lunt, E. Macusova, P.J. McCarthy, G. Pautasso, G.I. Pokol, G. Por, P. Svensson, the ASDEX Upgrade team, and the EUROfusion MST1 team, J. Plasma Phys 87, 1 (2021).
[7] I.M. Pankratov, Plasma Phys. Rep. 22, 535 (1996).
[8] E.M. Hollmann, P.B. Parks, N. Commaux, N.W. Eidietis, R.A. Moyer, D. Shiraki, M.E. Austin, C.J. Lasnier, C. Paz-Soldan, and D.L. Rudakov, Phys. Plasmas 22, 056108 (2015).
[9] R.A. Tinguely, M. Hoppe, R.S. Granetz, R.T. Mumgaard, and S. Scott, Nucl. Fusion 59, 096029 (2019).
[10] Ya. M. Sobolev, Questions At. Sci. Technol 4, 108 (2013).
[11] M. Hoppe, O. Embreus, R.A. Tinguely, R.S. Granetz, A. Stahl, and T. Fulop, Nucl. Fusion 58, 026032 (2018).
[12] L. Carbajal and D. Del Castillo-Negrete, Plasma Phys. Control. Fusion 59, 124001 (2017).
[13] K.C. Westfold, Astrophys. J. 130, 241 (1959).
[14] J. L. Luxon, Nucl. Fusion 42, 614 (2002).
[15] E.M. Hollmann, I. Bykov, N.W. Eidietis, J.L. Herfindal, A. Lvovskiy, R.A. Moyer, P.B. Parks, C. Paz-Soldan, A.Yu. Pigarov, D.L. Rudakov, D. Shiraki, and J. Watkins, Phys. Plasmas 27, 042515 (2020).
[16] A. Stahl, M. Landreman, G. Papp, E. Hollmann, and T. Fulop, Phys. Plasmas 20, 093302 (2013).
[17] L. Carbajal, D. del Castillo-Negrette, D. Spong, and L. Baylor, Phys. Plasmas 24, 042512 (2017).
[18] M. Hoppe, “Simulation and analysis of radiation from runaway electrons”, Licentiate thesis (2019).
[19] P.B. Parks and W. Wu, Nucl. Fusion 51, 073014 (2011).

[20] E.M. Hollmann, N.W. Eidietis, J.L. Herfindal, P.B. Parks, A.Yu. Pigarov, D. Shiraki, M.E. Austin, L. Bardoczi, L. Baylor, I. Bykov, T.N. Carlstrom, D. Kaplan, C.J. Lasnier, A. Lvovskiy, A. Moser, R.A. Moyer, C. Paz-Soldan, D.L. Rudakov, C. Samuell, M. Shafer, M. Van Zeeland, A. Welander, and R. Wilcox, Nucl. Fusion 59, 106014 (2019).
[21] https://fusion.gat.com/global/D3D_DMP.